Delft University of Technology

Introducing a comprehensive physics-based modelling framework for tandem and other PV systems

Vogt, M. R.; Tobon, C. Ruiz; Alcañiz, A.; Procel, P.; Blom, Y.; El Din, A. Nour; Stark, T.; Wang, Z.; Goma, E. Garcia; Etxebarria, J. G.

Introducing a comprehensive physics-based modelling framework for tandem and other PV systems

M.R. Vogt [*], C. Ruiz Tobon, A. Alcañiz, P. Procel, Y. Blom, A. Nour El Din, T. Stark, Z. Wang, E. Garcia Goma, J.G. Etxebarria, H. Ziar, M. Zeman, R. Santbergen, O. Isabella

Delft University of Technology, PVMD, Mekelweg 4, 2628CD, Delft, the Netherlands

ARTICLE INFO

ABSTRACT

We introduce a novel simulation tool capable of calculating the energy yield of a PV system based on its fundamental material properties and using self-consistent models. Thus, our simulation model can operate without measurements of a PV device. It combines wave and ray optics and a dedicated semiconductor simulation to model the optoelectronic PV device properties resulting in the IV-curve. The system surroundings are described via spectrally resolved ray tracing resulting in a cell resolved irradiance distribution, and via the fluid dynamics-based thermal model, in the individual cell temperatures. A lumped-element model is used to calculate the IV-curves of each solar cell for every hour of the year. These are combined factoring in the interconnection to obtain the PV module IV-curves, which connect to the inverter for calculating the AC energy yield. In our case study, we compare two types of 2 terminal perovskite/silicon tandem modules with STC PV module efficiencies of 27.7% and 28.6% with a reference c-Si module with STC PV module efficiency of 20.9%. In four different climates, we show that tandem PV modules operate at 1–1.9 °C lower yearly irradiance weighted average temperatures compared to c-Si. We find that the effect of current mismatch is significantly overestimated in pure optical studies, as they do not account for fill factor gains. The specific yields in kWh/kWp of the tandem PV systems are between -2.7% and $+0.4\%$ compared to the reference c-Si system in all four simulated climates. Thus, we find that the lab performance of the simulated tandem PV system translates from the laboratory to outdoors comparable to c-Si systems.

1. Introduction

To achieve climate neutrality the energy sector must switch to renewable energies. Scientific studies modelling 100% renewable energies scenarios by 2050 project that a solar photovoltaic (PV) capacity between 20 and 70 TWp needs to be installed within the next 30 years [1,2]. The production of such large amounts of PV modules is resource-intensive, especially with respect to glass and silver consumption, for these materials the PV industry might consume more annually than their current production capacity [3]. Pathways to solving this lack of resources can be found in a combination of reducing the use of these materials and increasing the operating efficiency of PV systems [3]. Thus, increasing solar system operating efficiency is a key factor in combating climate change.

In 2020, c-Si modules had a market share of about 95%, with stabilized mass production cell efficiencies up to 24% [4] under Standard Testing Conditions (STC: 25 °C, 1 kW/m^2, AM1.5g) [5]. Silicon solar cells produced for research and development have achieved efficiencies up to 26.7% [6,7], which is even closer to their theoretical efficiency limit of 29.4% [8,9] under STC. Thus, researchers are investigating alternative technology concepts, which can go beyond this limit. The perovskite/silicon tandem technology [10] has demonstrated a cell efficiency as high as 31.25% [11] in the laboratory. The technology has much room for further development as its fundamental limit is at 45% [12–14] and is expected to enter mass production in 2023 [4]. For a successful market entry, this tandem concept does not just need to demonstrate high efficiencies under STC, but also high energy yields in different climates to be bankable to investors and beneficial in combating climate change.

However, the conventional energy yield prediction tools currently (e. g. PVsyst [15], HelioScope [16], Solar Monkey [17], Plant predict [18], PV*Sol [19], System advisor model (SAM) [20]) do not cover tandem

---

* Corresponding author.
E-mail address: m.r.vogt@tudelft.nl (M.R. Vogt).

Table 1

Overview of which modelling features are considered fully (green), considered partly (yellow), taken from measurements (red), or not considered (red). The top six rows list several energy yield modelling software programs. The other rows studies predicting the energy yield of perovskite/silicon tandem cells, modules, or systems.

Name	1)Optical device	2)Semi-conductor device	3)Module mounting conditions	4)Spectrally resolved irradiation	5)Module thermal	6)Module electrical	7)DC to AC conversion
PVSyst[15]	*Measured*	*Measured*	**Yes**	Spectral coefficients	**Yes**	**Yes**	**Yes**
HelioScope [16]	*Measured*	*Measured*	**Yes**	Spectral coefficients	**Yes**	**Yes**	**Yes**
Solar Monkey [17]	*Measured*	*Measured*	**Yes**	Spectral coefficients	**Yes**	**Yes**	**Yes**
Plant predict [18]	*Measured*	*Measured*	**Yes**	Spectral coefficients	**Yes**	**Yes**	**Yes**
PV*Sol [19]	*Measured*	*Measured*	**Yes**	Spectral coefficients	**Yes**	**Yes**	**Yes**
SAM[20]	*Measured*	*Measured*	**Yes**	Spectral coefficients	**Yes**	**Yes**	**Yes**
Futscher et al. [12]	*Measured*	*Measured*	*No*	*Measured*	*Measured*	**Yes**	*No*
Dupré et al. [13]	Idealized	Idealized	*No*	**Yes**	**Yes**	*No*	*No*
Jäger et al. [14], [21]	**Yes**	Idealized	**Yes**	*Measured*	*No*	*No*	*No*
Hörantner et al. [22]	**Yes**	*Measured*	Tilt, no geometry	*Measured*	*No*	*No*	*No*
Jošt et al. [10]	Cell level only	*Measured*	Tilt, no geometry	*Measured*	*No*	*No*	*No*
Tucher et al. [23]	**Yes**	*Measured*	*No*	**Yes**	*No*	*No*	*No*
Singh et al. [24]	**Yes**	*No*	**Yes**	**Yes**	*No*	*No*	*No*
Schmager et al. [25],[26]	**Yes**	*Measured*	**Yes**	**Yes**	Empirical model	*No*	*No*
Julien et al. [27]	**Yes**	*Measured*	**Yes**	**Yes**	Empirical model	*No*	*No*
This work	**Yes**	**Yes**	**Yes**	**Yes**	**Yes**	**Yes**	**Yes**

devices. Their irradiation models are monochromatic with spectral correction coefficients, which would need to be adjusted for multi-junction cells. Additionally, they require measurements of fabricated devices optical and semiconductor behavior as input to model the energy yield.

In recent years, the research community has taken a high level of interest in predicting the energy yield of the perovskite/silicon tandem technology. In contrast, to the commercial software solutions they all use spectrally resolved irradiation either from measurements or modelling. However, as listed in Table 1 they do not cover all the steps traditionally included in energy yield modelling software.

Fundamental studies [12–14] into the energy yield of perovskite/silicon tandems identified that the ideal band gap for the

perovskite top cell is 1.73–1.74 eV for a monofacial two terminal cells and 1.82 eV for a monofacial four terminal cells. These studies assume idealized cells based on the detailed balance limit [28].

Several studies [22–24,29] used realistic models to simulate the optical material properties based on wave optics to optimize the optical properties of the perovskite/silicon tandem solar cells in realistic conditions. However, the models in these studies did not include the thermal behavior of the solar cells.

The models by Schmager et al. [25] and Julien et al. [27] included empirical module temperature models and are able to calculate the energy yield of perovskite/silicon tandem solar cells in realistic conditions. They both build on the four same pillars: (a) Optical device simulation with wave optics and ray tracing, (b) typical meteorological
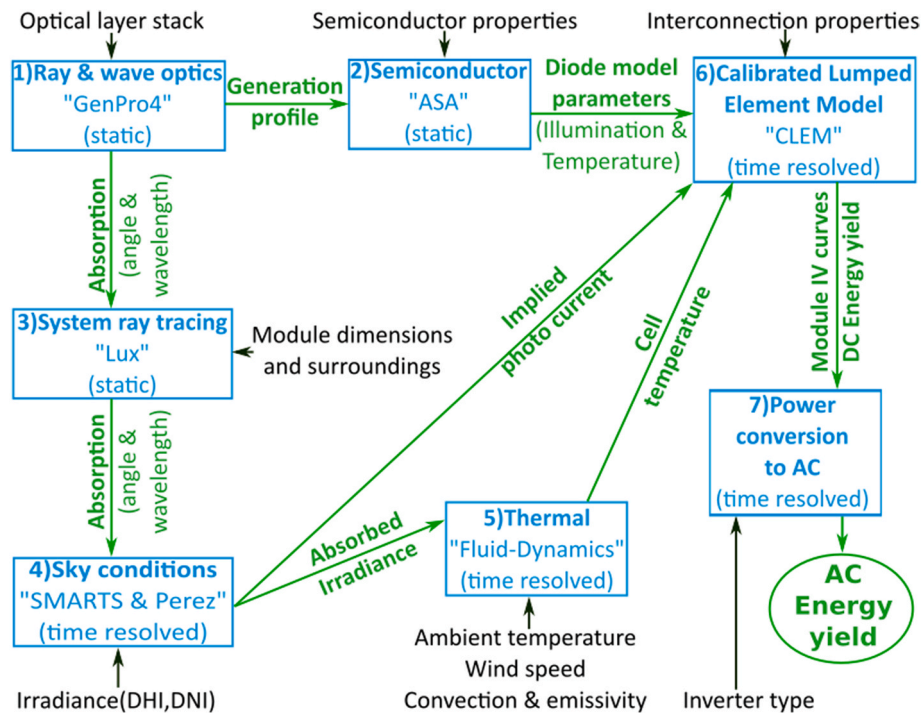

Fig. 1. Flowchart of PVMD Toolbox describing the simulation methodology. The input data is indicated in black. The main models and (intermediated) results are in blue and green, respectively. (For interpretation of the references to color in this figure legend, the reader is referred to the Web version of this article.)
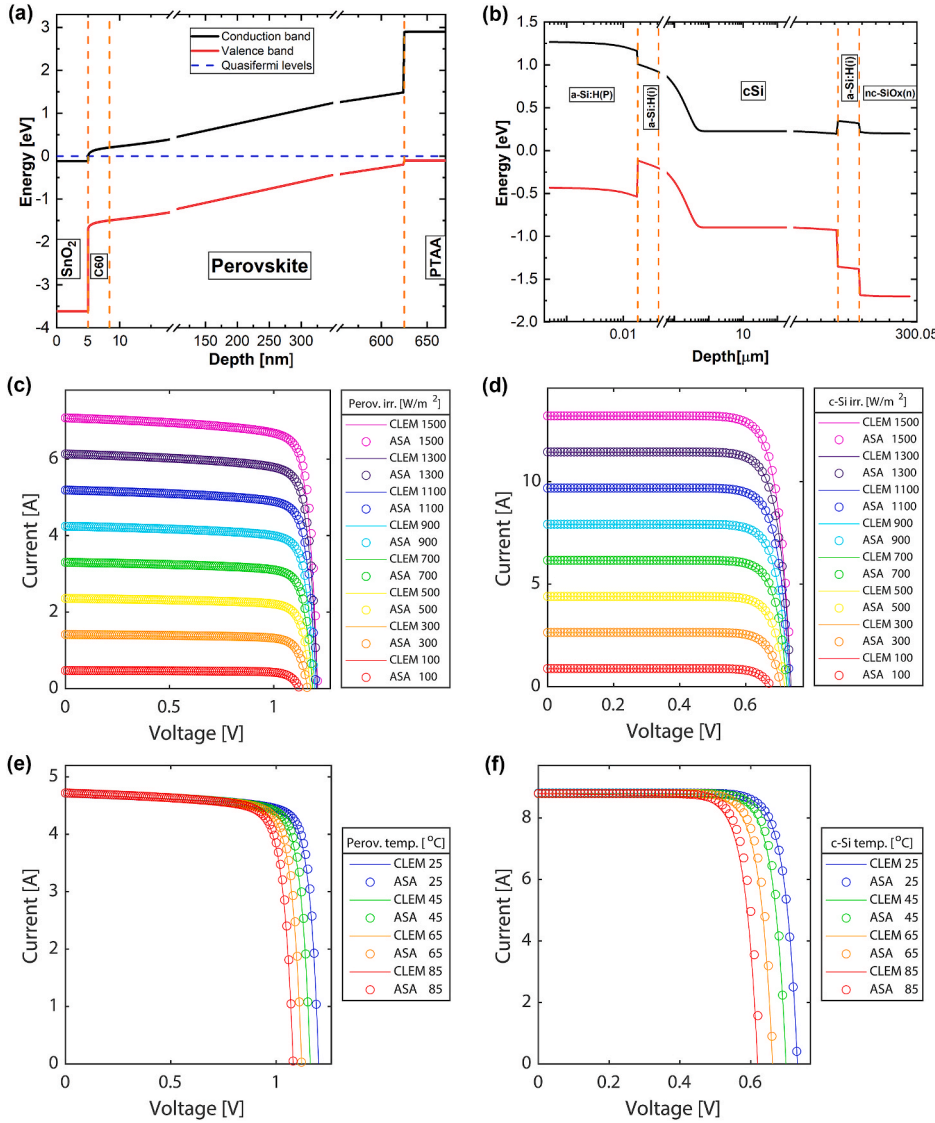
Fig. 2. The perovskite top cell is always shown on the left, while the silicon heterojunction bottom cell is shown always on the right. Band diagrams as simulated by ASA for both cells are shown in the top row. Irradiance dependence of the IV-curves for both ASA and CLEM are shown in the middle row. Temperature dependence of the IV-curves for both ASA and CLEM are shown in the bottom row. (For interpretation of the references to color in this figure legend, the reader is referred to the Web version of this article.)

year (TMY climate data enhanced by spectra from SMARTS [30,31], (c) an empirical temperature model and (d) the one diode model with input from IV-curve parameters from tandem cells measured in the laboratory to calculate the energy output of effectively a one solar cell module. This four step approach requires devices to be fabricated in order to determine the new electrical and thermal parameters and ultimately determine the impact any changes on operating temperature and electrical power output. Furthermore, these models do not consider a full PV module with more than one solar cell. Thus, interconnection in a module and especially differences in irradiation onto the different cells cannot be simulated. Additionally, the DC to AC conversion is not currently included in these models.

In this work, we introduce a new model called "PVMD Toolbox," which includes semi-conductor device modelling it energy yield modelling. This makes our software unique in the fact that it can simulate PV systems AC energy yield based on fundamental material parameters. In comparison with previous models [25–27], we add electrical device modelling, a non-empirical temperature model, electrical interconnection of a full industrial size PV module with more than one solar cell (typically 72 cells) and DC to AC conversion. Thereby, our model can simulate the AC energy yield even if no such solar cell or module was fabricated. This enables fast investigations with many variations to see how changes in one layer impact the final AC energy

yield. As a consequence, the speed of the development process can be increased, and additional insights can be obtained.

The focus of this paper is the introduction of the new model and validation (section 2). In section 3, we demonstrate the capabilities of our model in a case study comparing to two tandem systems with a c-Si reference in four different climate types. Finally, we summarize and conclude our work (section 4).

2. Simulation model

The flowchart of the simulation model for energy yield calculation in the PVMD TOOLBOX is shown in Fig. 1, with the main models (blue), the information flow as well as the (intermediate) results (green) and the input (black). The PVMD TOOLBOX extends scientific yield prediction models for tandem solar cells to seven pillars. Pillar **1)** considers ray and wave optics in the module layer stack described by the materials' complex refractive indices. It calculates spectral, depth and angle dependent absorption for each layer in the cell. The generation profile serves as an input for pillar **2)**, the advanced semiconductor analysis software, which is used to calculate the cell IV-curves at different irradiances and temperatures for the toolbox. An equivalent circuit model of the solar cell, is then fit to match all the IV-curves, resulting in a calibrated lumped-element model with temperature and illumination
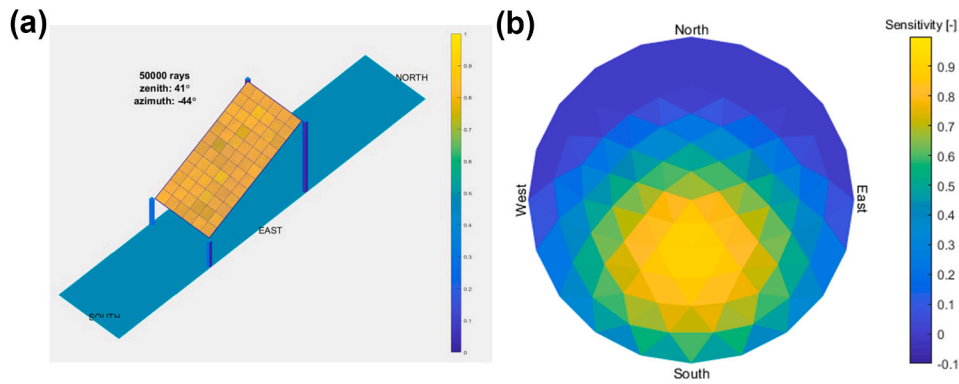
Fig. 3. Periodic simulation domain for ray tracing (a). Geometrical features of the module, its mounting conditions and the surroundings are considered as well as their optical properties. Resulting sensitivity map can be calculated for each cell (b).

dependent parameters. The first pillar results also serve as an input for pillar **3)**, system level ray tracing, which simulates the PV module mounting conditions and surroundings allowing for shading and albedo effects to be considered, resulting in a sensitivity map of the PV system. Together with pillar six, these models give us a static description of the PV system from fundamental material properties to module IV-curves.

Pillar **4)**, the first time resolved step, is the creation of a distribution of the radiance across the sky based on the Perez model and SMARTS to add the spectral information. Afterwards, integrating the sensitivity and sky maps results in the irradiance absorbed by the module and the cell photo currents. The former is used in pillar **5)** together with ambient temperature, wind speed, convective heat loss and emissivity for the fluid dynamic model implemented in the toolbox to calculate the temperature of each cell in the module. Next in pillar **6)**, a lumped-element model is used to simulate the module interconnection in combination with the calibrated lumped-element model parameters and the resulting module IV-curve for all timesteps considering the temperature and implied photo current for each cell at each timestep of the simulation time (typically one year). Afterwards, in pillar **7)** the DC power is converted to AC considering voltage and current dependent efficiency of the inverter for each timestep. In the following, we will introduce each model in detail.

2.1. Optical model for PV module properties

The solar modules' optical properties are simulated using the GEN-PRO4 software [32]. GENPRO4 implements the net radiation method [33] and further extended versions of that [34,35]. The original net radiation method approximates the cell structure as a 1-D multilayer stack along the depth axis of the cell. The thickness d and complex refractive index n (λ), $k(\lambda)$ of every layer are input parameters. The extended models allow for interference and scattering effects to be considered. Random surface textures are simulated using the scalar scattering model developed by Jäger et al. [36], which utilizes a 3D scan by an atomic force microscope to model a realistic texture.

As part of the PVMD TOOLBOX, GENPRO4 calculates spectral and angle resolved reflection $R_{mod}(\lambda, \alpha)$ as well as absorption which is also depth resolved $A_{lay}(\lambda,\alpha,d)$ for each layer in the module including the cell with all its layers. In case of a bifacial structure this calculation is performed for front as well as rear irradiation. This approach has demonstrated very good agreement with measurements in various publications such as [32,34–36].

2.2. Semiconductor device model

The ADVANCED SEMICONDUCTOR ANALYSIS (ASA) is an optoelectronic simulator program from Delft University of Technology [37–39]. It solves the semiconductor equations in one dimension, specifically the Poisson equation and two continuity equations for electrons and holes.

The physical background is based on the drift-diffusion model consistently coupled with recombination and tunneling models. ASA accounts semiconductor electronic properties such as bandgap, electron affinity, density of states, mobility, doping profiles and trapped charges in the localized states within the band gap to simulate one-dimensional devices under various illumination or dark conditions, all as a function of temperature. Each material's free electron concentration, hole concentration, electrostatic potential and depth resolved generation profile $A_{lay}(\lambda, d)$ are input variables for ASA. Fig. 2a shows an example of resulting band diagrams for a perovskite top and Fig. 2b a silicon heterojunction bottom cell.

As part of the PVMD TOOLBOX, ASA is used to calculate the cell IV-curves at different irradiances and temperatures. To save computational effort an equivalent circuit model of the solar cell is then fitted to match all the IV-curves. This way we obtain a calibrated lumped-element model (CLEM) with temperature and illumination dependent parameters of the one diode model for the solar cell. Fig. 2c–f show the comparisons between ASA and CLEM. Note, that the top and bottom cell one diode model parameters are extracted separately and then later combined in an equivalent circuit model for each tandem solar cell with either series connection or independent operation subject to the number of terminals of the cell.

2.3. Optical model for module mounting conditions

The in-house developed forward Monte-Carlo ray tracing software LUX is used to simulate the PV module mounting conditions and surroundings allowing for shading and albedo effects, especially important for bifacial modules, to be considered. The ray-tracing method was chosen for its flexibility as it can treat complex illumination situations, including shading and light scattering from nearby objects. The optical properties of these nearby objects, such as spectral reflectance and diffuseness of reflection, can be chosen freely, to closely mimic the real-world situation. Note that commonly used methods based on view factors require less computation time but are based on the assumption that surfaces reflect light in a perfectly diffuse way.

The simulation domain is shown in Fig. 3a, it simulates a single PV module with periodic boundary conditions on four sides representing a module in a large PV power plant. The module is modelled considering the size of each cell, the tilt, the mounting height, the frame, the distance between cells as well as the frame and the distance to other modules. The reflection and absorption properties of the PV module are based on the simulation as described in section 2.1. The ground is modelled with a reflectivity and two factors, which adjust the haze and diffuse exponent of the ground reflection. The result are sensitivity maps [40] as shown in Fig. 3b and defined by

$$S_l\left(n_{cell},\ \vartheta_{in},\ \varphi_{in}, \lambda_{in}\right) = \frac{N_{abs,l}(n_{cell},\ \vartheta_{in},\ \varphi_{in}, \lambda_{in})}{N_{in}}, \tag{1}$$
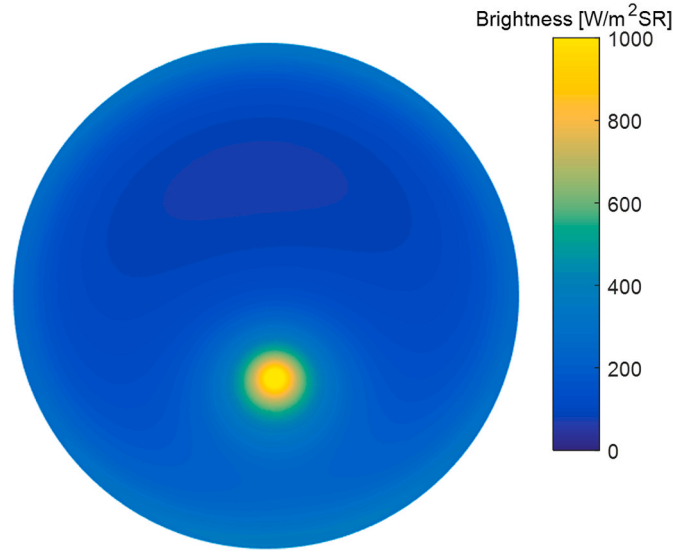
Fig. 4. Irradiance map showing the irradiance distribution across the sky for one-time instance.

where N_{in} is the number of incoming rays per simulation step, $N_{abs,l}$ is the number of absorbed rays, n_{cell} is the cell number in the module, θ_{in} zenith angle, φ_{in} azimuth angle, λ_{in} wavelength, S_l is the sensitivity and l is the layer in the module. Typically, one sensitivity map is calculated for each junction (jnc) material as basis to calculate their current and another one for the whole module to derive the input for the module temperature model.

2.4. Time and spectral resolved irradiance model

The first time resolved calculation step is the creation of a distribution of the irradiance across the sky in the time domain. The model is based on the Perez model [41]. Fig. 4 shows an example of such an irradiance map. Then, the model uses SMARTS [42,43] to add the spectral composition of the incoming G irradiance or the incoming φ photon flux. The former is used for the module temperature calculation while the latter is used for the current calculation.

Objects on the horizon such as mountains or large buildings are considered by a shading factor, which multiplies the direct normal irradiance (DNI) with zero in instances when the sun is behind these objects.

Afterwards we integrate the sensitivity and irradiance maps over all wavelengths, zenith, and azimuth angles according to

$$G_{mod}(n_{cell}, t) = \iiint S_{mod}(n_{cell}, \vartheta_{in}, \varphi_{in}, \lambda_{in}) \times G(t, \vartheta_{in}, \varphi_{in}, \lambda_{in}) \, d\vartheta \, d\varphi \, d\lambda, \quad (2)$$

$$I_{jnc}(n_{cell}, t) = \iiint S_{jnc}(n_{cell}, \vartheta_{in}, \varphi_{in}, \lambda_{in}) \times \Phi(t, \vartheta_{in}, \varphi_{in}, \lambda_{in}) \times e \, d\vartheta \, d\varphi \, d\lambda. \quad (3)$$

The results are G_{mod} the irradiance absorbed by the module block enveloping each cell including half of the inter cell gap as well as I_{jnc} the implied cell photo-generated currents for each cell, time instance and junction, while e is the elementary charge. The former is an input variable for the module temperature calculation, while the latter is an input variable in the electrical model.

2.5. Thermal model

The PVMD TᴏᴏLʙᴏx uses a fluid dynamic model [44] to calculate the temperature of each cell in the module. It considers natural as well as forced convection and radiative heat transfer for all time instances. The input parameters are ambient temperature, wind speed, module
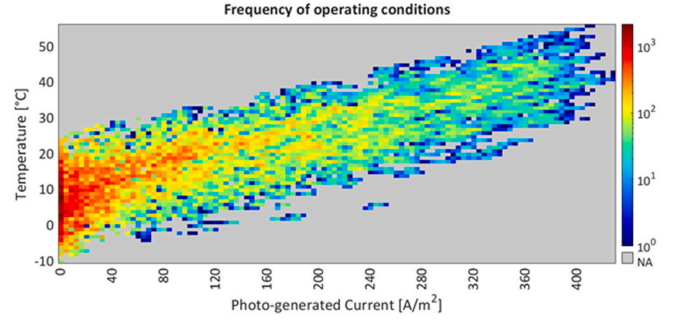

Fig. 5. Frequency of solar cell operating conditions as function of cell temperature and photo generated current for one year in hourly resolution in Delft. The rectangles show how these operating conditions are organized into these colored rectangles. Note, that for illustration purposes the rectangles shown here are 33.3 times larger than the ones typically used in our simulations.

efficiency at STC, temperature coefficient of the efficiency, sky temperature, module tilt, module mounting height, emissivity of the module and the irradiance absorbed by the module G_{mod} (n_{cell},t) derived as described in the previous section. The output is the temperature of each cell in the PV module at each time T_{cell} (n_{cell},t). Note, that this fluid dynamic model relies only on non-empirical parameters and is thus able to directly include the impact of a different efficiency or other property on the operating temperature whereas previous works are based on empirical temperature models [20,21]. For example, if you simulate yet to be fabricated tandem modules then you do not need to first determine their empirical temperature parameters.

2.6. Module electrical interconnection model

Next, the PVMD TᴏᴏLʙᴏx uses a lumped-element model to simulate the module interconnection with bypass diodes to calculate the resulting module IV-curves for all hours of the year. The first step is calculating the time resolved IV-curves for each cell. Using the lambert W function approach [45], we speed up the simulation process to the point where we can calculate a 100 000 IV curves per minute. The inputs are the implied cell photo-generated currents $I_{jnc}(n_{cell}$,t), the cell temperature $T_{cell}(n_{cell}$,t) and the temperature and illumination dependent parameters of the one diode model all derived as describe in the previous sections.

If we simulate a module with 60 cells for one year in hourly resolution then several hundred thousand IV-curves need to be calculated, even if we exclude night times with zero irradiance. However, as shown in Fig. 5, a lot of solar cell operating conditions in terms of cell temperature and implied photo generated current are repeated several hundred times. Thus, we organize the operating conditions in discrete cell temperature steps of $\Delta T_{cell} = 0.3$ K and implied photo generated current steps of $\Delta J_{ph} = 0.4$ A/m^2 and only simulate each of those discrete condition steps once if they appear in the climate. For simulating one year in Delft (Netherlands) in hourly resolution, this reduces the amount of simulated IV-curves for a 60-cell module by 86% and the simulation time to about 2 min on a desktop PC (3 GHz, 8 GB RAM). The specific reduction depends on the climate conditions at the location and the number of cells in the module. The computational effort reduction scales extremely well with higher time resolution of the climate data or simulating multiple years, as the number of unique operating condition steps hardly increases, only the frequency in each step. However, comparing a simulation with these discrete operating steps and without them the calculated yearly module yield is overestimated by 0.23% in this example. The overestimation is due to a reduction in slight current mismatch losses. The overestimation scales with step size as larger step sizes decrease current mismatch losses, thus we always have a trade-off between speed and accuracy when using this approach of organizing operating conditions in discrete steps.
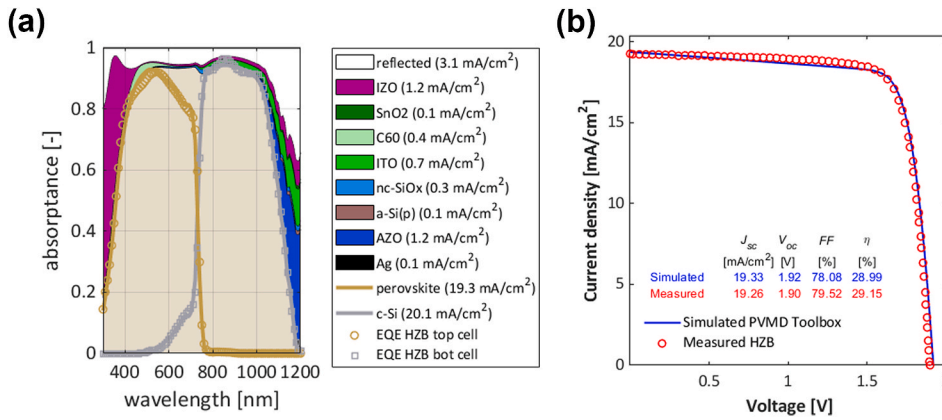
(a)

(b)

Fig. 6. The symbols mark measurements of the 29.15% efficiency perovskite/silicon tandem device fabricated by HZB [50]. On the left, the measured EQE for top and bottom cell is compared to the PVMD Toolbox optical device simulation of this structure. The inputs are listed in Appendix A. On the right, the measured JV curve is compared to the JV curve as simulated by the PVMD Toolbox. (For interpretation of the references to color in this figure legend, the reader is referred to the Web version of this article.)

2.7. Inverter model

Afterwards, the DC power is converted to AC considering voltage and current dependent efficiency of the inverter for each time-step. The input variables are the DC current and voltage of the module for each timestep from the pervious calculation step. The input parameters are the number of modules in series and parallel connection, the DC and AC cable as well as the inverter properties. The PVMD Toolbox can simulate PV systems with central inverters, string inverters, micro inverters, and power optimizers. For the three inverter types, conversion efficiencies are calculated based on the SNL-model [46]. For power optimizers, we built our own model based on efficiencies measured as a function of input power at different input voltage levels [47]. The yearly inverter efficiencies for the PV system considered in this paper are 93.7–95.5%.

2.8. Validation in standard test and realistic conditions

The individual calculation steps have shown close agreement with measurements in literature e. g. Refs. [32,37,40,44–47]. The self consistent combination of these models is able to do the same.

News of the record 31.25% [11] and 29.80% [48] perovskite/silicon tandem cells was published after this study was already finished and there was also not enough information available to model the previous Oxford PV record device with 29.52% efficiency [49]. However, HZB who fabricated a previous perovskite/silicon record device with 29.15% efficiency have published detailed information on their device [50], which will be used for validation. The symbols in Fig. 6a mark measurements of this device as digitally extracted from Ref. [50]. The measured EQE for top (yellow) and bottom (grey) cell is compared to the PVMD Toolbox optical device simulation of this structure. The mean absolute deviation between simulation and measurement is 1.1% for the top cell and 0.9% for the bottom cell. The simulated implied photo generated current densities are also within 0.1 mA/cm^2 of the measured short circuit current densities. Fig. 6b shows the measured JV curve (red symbols) is compared to the one obtained via the PVMD Toolbox opto-electrical device modeling with a mean absolute deviation below 0.3 mA/cm^2 (1.6%). Thus, our steady state model can accurately model lab measurement of perovskite/silicon tandems.

As no data of detailed outdoor energy yield measurements of perovskite/silicon tandem modules is currently available in literature, we validate the transition from STC to outdoor conditions with such data from c-Si modules. Marion et al. [51] published open source data of PV module outdoor performance. We model the 72-cell HIT module and its mounting conditions in the PVMD toolbox, import measured DHI, DNI, ambient temperature and wind speed data recorded for a 13-month period with a 10-min resolution in Cocoa, Florida. Comparing the measured PV DC power with the modelled one we determine a root mean square difference of 4.5% and a mean bias difference of −4.2%.
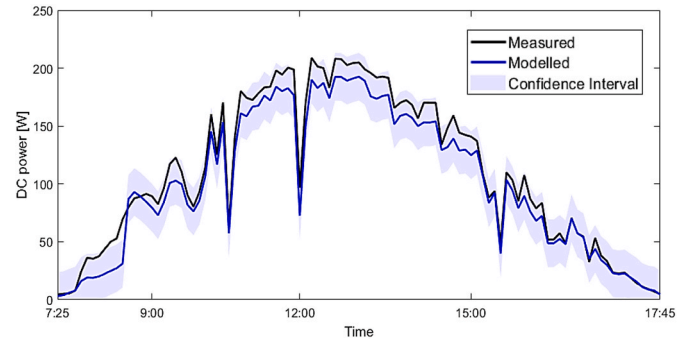

Fig. 7. Modelled PV DC power output (blue line), 95% confidence interval (blue area) and measured PV DC power output (black line) [51]. Even on February 11, 2011, the day with the highest deviation, the measured data is within the confidence interval of our model. (For interpretation of the references to color in this figure legend, the reader is referred to the Web version of this article.)

The mean bias difference is calculated as the sum over the differences between predicted and measured yield for all time steps divided by the total measured energy yield. Therefore, a negative value means that our model has a slight bias towards underestimating the measured energy yield, the source of this slight underestimation bias is unknown. Fig. 7 shows the day with the highest deviation between modelled PV DC power output (blue line) and measured PV DC power output (black line). Even on this day the measurement is nearly always in the 95% confidence interval (blue area) of our model.

3. Results

In the following, we conduct a case study to analyze how the transition from nominal STC power to actual power in real-world operation comapres for tandem PV systems and conventional c-Si systems. This can best be evaluated by comparing the specific yields of these systems as calculated by the PVMD Toolbox for different climates.

To simulate realistic modules, we assume the encapsulation of these perovskite/silicon tandem cells from Ref. [50] with 450 μm polyolefin without UV blocking additives and 3.2 mm thick sola lime glass with an iron content of 10 ppm [52]. The glass has a double layer anti-reflection coating (ARC) with 93 nm Teflon AF2400 [53,54] on top of 53 nm porous glass ARC layer [55]. We remove LiF layer on top of the solar cell, which is an optimization for a having low reflection in air rather than in a glass/polyolefin stack with refractive indexes around 1.5. As can be seen in Fig. 6a, the reference device is not current matched perfectly, as the c-Si bottom cell has a 0.8 mA/cm^2 higher implied J_{sc} than the top cell and the encapsulation in a PV module changes that balance further. We reduce the c-Si wafer thickness to 160 μm in all our simulations in the

Table 2

Overview of the main cell and module properties for the double textured c-Si as reference, the rear texture 2-Terminal tandem (2T-RT) and the double texture tandem (2T-DT). The silicon wafer thickness is fixed to 160 μm, which is a typical value for today's industrial c-Si solar cells, and the perovskite thickness is adjusted to achieve current matching in the module under STC. An extended version is in appendix A.

Cell type	Cell texture	Perovskite thickness [μm]	Silicon thickness [μm]	Power STC [W]	Module efficiency STC [%]
c-Si	Double	NA	160	394	20.9
2T-RT	Rear	0.575	160	521	27.7
2T-DT	Double	0.48	160	540	28.6

results section and fit the perovskite thickness to achieve current matching. We consider a bottom cell rear textured device with a planar perovskite top cell with thickness of 575 nm and a double textured device, which has also a texture on the front side of the bottom cell, this texture with pyramid size of typically 5 μm makes the perovskite top cell textured. To adjust for the better light trapping due to the double texture the perovskite thickness is adjusted to 480 nm, otherwise both 2T cells are identical. Table 2 lists the STC power and efficiency values for those two devices as well as a device based on the bottom cell of the double textured variant encapsulated in a module with the same materials as a reference.

3.1. Loss analysis under standard test conditions

To evaluate the design of the solar cell, module, and system, it is important to know which factors limit the efficiency the most. Thus, our simulation software can perform a loss analysis quantifying the different losses that are present. There are 17 losses defined, which are grouped into four categories. These categories are fundamental, optical, electrical, and system losses. The fundamental losses are calculated first, such that they give an upper limit for the solar cell. For the calculation of the fundamental losses, an ideal solar cell is assumed. The results of our fundamental losses match the upper limits for both single junctions as tandem cells [28,56].

Additional to the five fundamental losses, a non-ideality effect has been defined to compensate for an overestimation of the fundamental losses. This non-ideality component considers the absorption of photons below the bandgap energy, also known as Urbach's rule [57], and the fact that the actual emission is lower if the solar cell is not ideal.

After the fundamental losses, the optical losses are calculated. This category accounts for all the photons that impinge on the PV module but are not able to generate an electron-hole pair. This includes non-active

area losses, and reflection or parasitic absorption. The reflection and parasitic absorption are calculated based on the results of the optical model.

The electrical losses consist of two different losses: ohmic losses, and recombination losses. The ohmic losses are calculated with the series resistance and the shunt resistance of the five-parameter model. Recombination losses are the losses due to the recombination of electron-hole pairs. This recombination results both in a decrease of the maximum power point current and in a decrease of the maximum power point voltage. Therefore, the recombination is split into two components.

The last category is the system losses and includes all losses introduced by inserting the solar cells in a photovoltaic system. Two of the system losses are related to the connection of solar cells, which are ohmic losses due to the interconnection, and the mismatch losses. The mismatch losses are caused by different maximum power point conditions of the cells, such as due to current mismatch between the top and bottom cells or partial shading of the module. The other two system losses are related to the conversion from DC to AC, which are cable losses and inverter losses. However, for STC simulations the last two losses are not considered since STC is defined as module DC output.

The loss analysis has been simulated for the modules discussed above at STC. The results are shown in Fig. 8. The most significant difference is that the fundamental losses decrease for the tandem modules. This is expected since tandem modules are designed to reduce the thermalization losses. The emission losses increase for tandem modules, since there is a larger cell voltage for tandem modules, which increases the emission. The reflection losses are significantly higher for the two-terminal rear-textured tandem module since it is has a flat front interface. The parasitic absorption decreases for this module, which is the result of the increase in reflection.

The recombination losses are higher for the tandem modules because there is more recombination in these perovskite top cells. As can be seen in Fig. 2e and f, the perovskite cell has a lower fill factor than the silicon cell, implying that there is more recombination. The system losses are small for all modules, since the system has been optimized for the specific cells.

3.2. Outdoor yield simulation

We simulate the three different PV module types in four different climatic locations: i) Delft (Netherlands) representing temperate low irradiance climates (DL), ii) Shanghai (China) representing temperate medium irradiance climates (DM), iii) Lisbon (Portugal) representing temperate high irradiance climates (DH) and iv) Lagos (Nigeria) representing tropical high irradiance climates (AH). The hourly climate data is extracted from METEONORM version 7.3. Table 3 lists the annual or mean
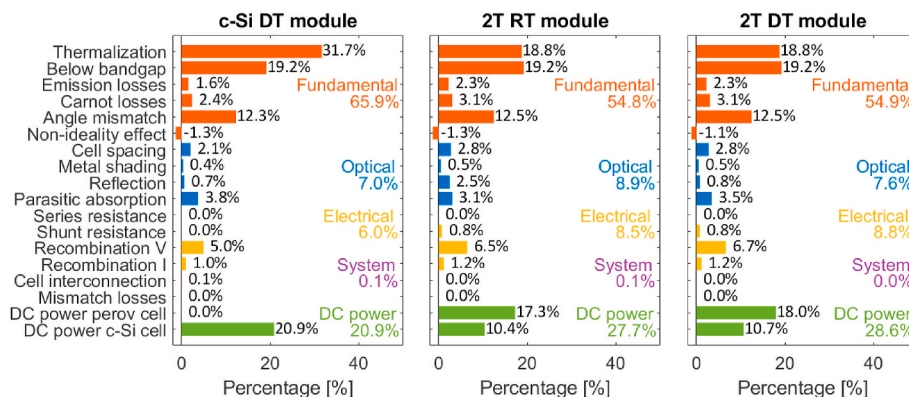

Fig. 8. The loss analysis for the c-Si DT module, the two-terminal rear-textured tandem module, and the two-terminal double-textured tandem module. The fundamental losses have decreased for the tandem modules, whereas the electrical losses have increased for the tandem modules. The optical losses are higher for the two-terminal rear-textured module since it does not have front texturing.

Table 3

Overview of the annual or mean annual global horizontal irradiation, ambient temperature and wind speed as well as the climate KGPV classification [58] and optimum tilt for each of the four climate data sets used in this work.

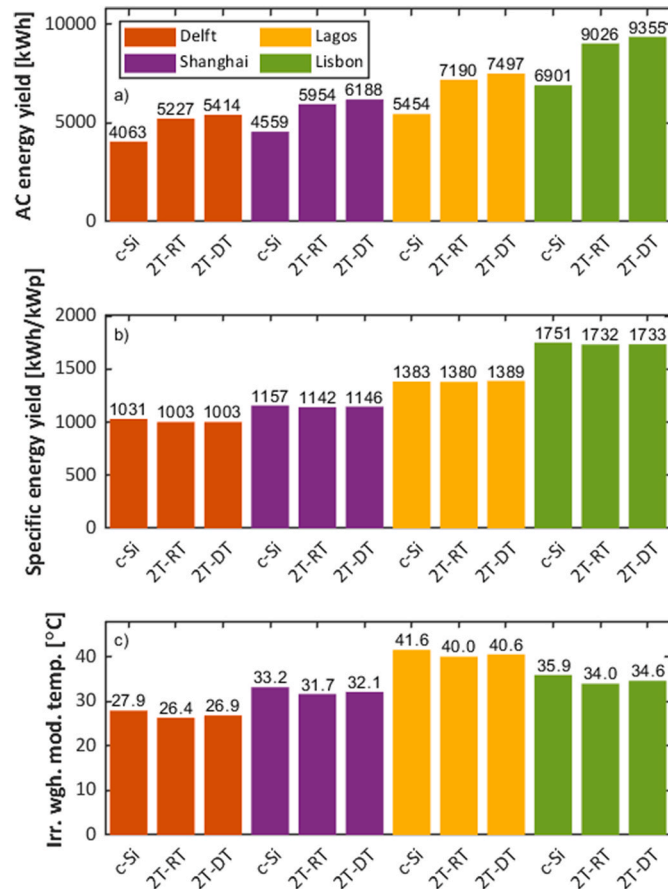| Location	Annual global horizontal irradiation [kWh/m^2]	Mean annual ambient Temperature [°C]	Mean annual wind speed [m/s]	KGPV	Optimum tilt [°]
Delft	1018	10.8	4.0	DL	31
Shanghai	1271	17.5	3.5	DM	17
Lagos	1642	27.5	3.9	AH	5
Lisbon	1758	16.7	3.6	DH	28

Fig. 9. a) The top plot shows the annual AC energy yield for each of the PV systems in all four locations. b) The middle shows the specific yield of all systems. c) The bottom plot shows the irradiance weighted mean of the annual module temperatures indicating that tandem systems operate at a about 1 °C lower temperature.

annual differences global horizontal irradiation, ambient temperature, wind speed and optimum tilts. The climates are categorized based on the Köppen-Geiger-Photovoltaic (KGPV) classification [58–60].

We simulate PV systems consisting of two parallel strings with five PV modules in series per string. Fig. 9 shows the results in terms of annual AC energy yield (a), specific system yield (b) and irradiance weighted mean annual module operating temperature (c) in all four climates.

The 2T-RT variant has a 29–32% higher AC energy yield than the c-Si reference, while the 2T-DT variant has a 33–37% higher AC energy yield compared to the reference. In both cases the improvement is lowest in the temperate low irradiance climate (Delft) and highest in the tropical high irradiance climate (Lagos).

The specific system yield is highest in Lisbon with a range from 1732

Table 4

Annual losses due to current mismatch between top and bottom cell. The current loss columns are the sum of the absolute hourly differences between top and bottom cell current relative to the sum of bottom cell currents. The power loss compares the sum of the sub cells individual MPPs and the MPPs of the 2T relative to the later, thus accounting for fill factor gains. The mismatch loss is taken from our loss analysis. Therefore, they are relative to the incoming power and not the device performance.

Climate	Variation	Short circuit current loss [%]	Current losses at MPP [%]	Power loss relative to DC power [%]	Mismatch losses relative to incoming irradiation [%]
Delft	2T-RT	7.0	6.5	1.2	0.3
Shanghai	2T-RT	6.9	5.3	0.8	0.2
Lagos	2T-RT	8.1	6.0	0.9	0.2
Lisbon	2T-RT	6.3	5.3	0.8	0.2
Delft	2T-DT	7.5	7.5	1.5	0.4
Shanghai	2T-DT	6.3	5.5	0.9	0.2
Lagos	2T-DT	6.8	5.3	0.7	0.2
Lisbon	2T-DT	6.5	6.1	1.0	0.3

to 1751 kWh/kWp and lowest in Delft with a range from 1003 to 1031 kWh/kWp. In terms of specific yield, the tandem system performs slightly worse than the c-Si reference module with -2.7% in Delft and about -1% in both Lisbon as well as Shanghai. In the tropical Lagos climate, we observe the 2T-RT variant is -0.3% below the specific yield of the c-Si reference, while the 2T-DT variant is +0.4% above of the specific yield of the c-Si reference.

The better performance in the tropical climates can be partly explained by the lower weighted mean annual module operating temperature, which is about 1 °C lower than the reference module for the 2T-DT and about 1.5 °C lower than the reference for the 2T-RT variant. The lower operating temperature of the tandem modules is mainly due to lower thermalization losses (see also Figs. 8 and 10). The difference between the tandem variants is due to the higher reflection of the 2T-RT variant, which leads to lower absorption in the module. Based on our ASA simulations, we can determine the temperature coefficient of the tandem cell, which equals -0.3%/K. This means that the specifical yield would be about 0.3% lower for the DT tandem and 0.45% lower for the rear textured tandem if they would operate at the same temperature as the c-Si.

The other factor affecting the specific yield is the spectral composition in the different climates across all hours of the year, which causes current mismatch losses between top and bottom cells. Table 4 lists the annual losses due to this current mismatch. Note that, we averaged across the whole module area for this analysis to eliminate the effect irradiation differences due to cell position. Comparing the current mismatch with the power mismatch loss we find a significant reduction. The reason is that fill factor gains compensate much of the current mismatch losses. This clearly shows the need to include electrical modelling when evaluating current mismatch losses. Location wise the mismatch losses are largest in Delft and lowest in Lisbon and Shanghai. This partly explanations, why the tandems specific yield is lower in Delft compared to the other locations. An additional factor is that all spectra have a blue shift compared to AM1.5g, specifically the blue shift is lowest in Delft and strongest in Lagos, which further explains why the specific yield of the tandems are particular high in this location. More details follow in the outdoor loss analysis in the next section.

We find that the lab performance of the simulated tandem system translates from the laboratory to outdoors within -2.7% to +0.4% the reference c-Si systems' specific yields for all four simulated climates. Note that the calculated performance ratio also depends on the spectral irradiance model used, which is still a topic with much research to be done before a consensus can be reached [61–64]. There is a clear need to further validate these findings with long-term measurement campaigns of perovskite/silicon tandem modules in different climates. However, currently no such data is available for perovskite/silicon tandem
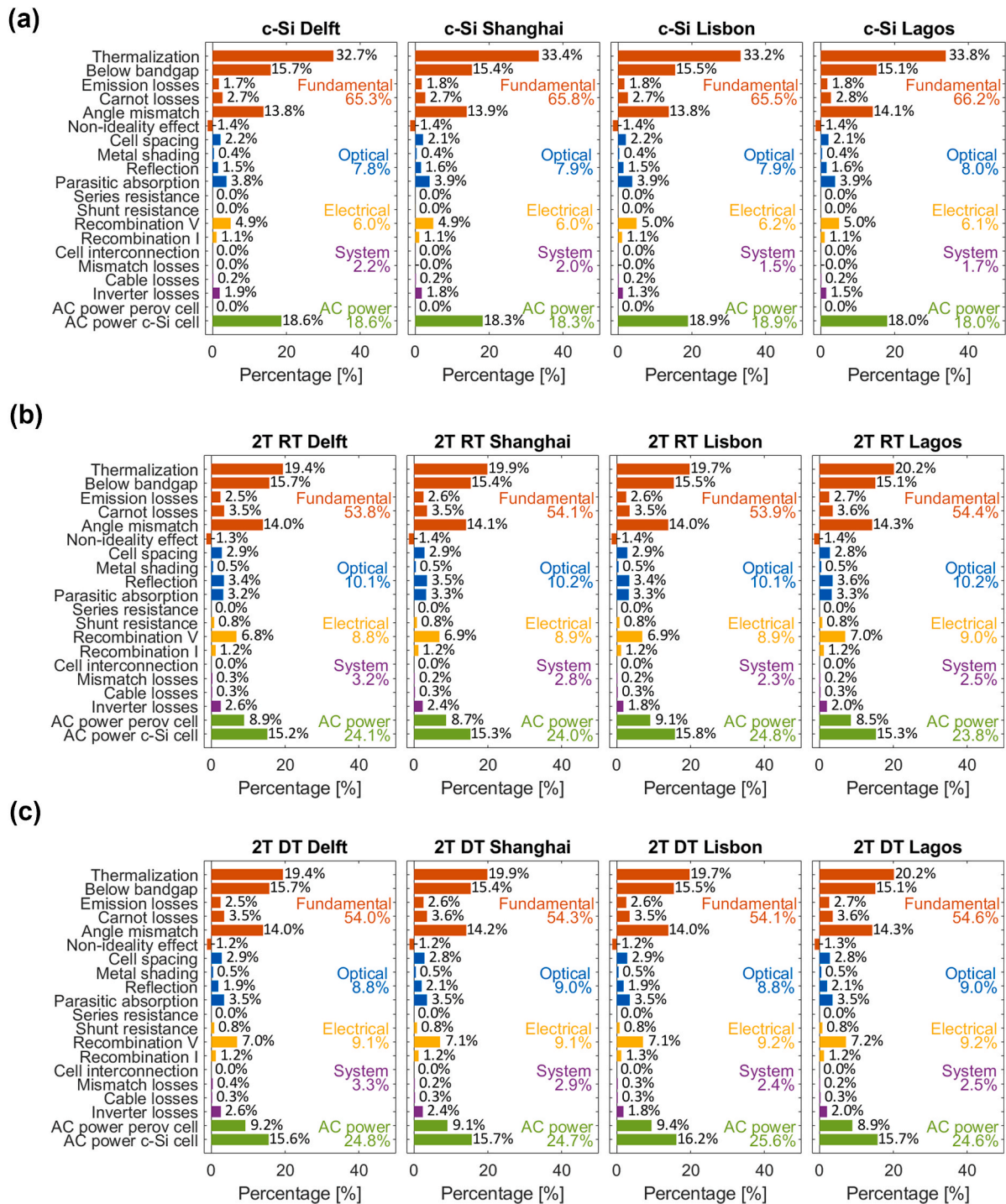
(a)

(b)

(c)

Fig. 10. The loss analysis for the three modules in the four operating climate locations. In a) the results of the c-Si modules are shown, b) shows the results for the rear textured tandem and c) shows the results for the double textured tandem.

modules. We are open to contribute our modelling to better understand such measurements and further improve our modelling, so please feel free to contact us if you have or plan to collect such data.

3.3. Outdoor loss analysis

The loss analysis described in section 3.1 is not only done for STC, but also for the varying real-world outdoor conditions for the locations Delft, Shanghai, Lagos, and Lisbon. The results accumulated over one year are shown in Fig. 10. They can be compared to the loss analysis at

STC, such that it can be seen how the actual operating conditions affect the performance.

The first difference that can be observed, is that the fundamental losses have changed. The below bandgap non-absorption has decreases from 19.2% at STC to values between 15 and 16%. The reason for this is that the spectra are blue shift compared to the AM1.5g spectrum, as mentioned in the previous section. This reduces the irradiance with energy below the energy bandgap of silicon. The below bandgap non-absorption is the lowest in Lagos, since this location has the strongest blueshift. Delft has the highest below bandgap non-absorption since it

has the weakest blue-shift. The blue shift also causes the increase of thermalization losses compared to STC, which is the highest in Lagos and the lowest in Delft. Explaining the different specific yield values in these locations.

Another difference compared to STC, is that the reflection and parasitic absorption have increased. This is due to more irradiance coming in at an oblique angle. The EQE of a solar cell is typically the highest when light reaches the cell at the normal angle. However, under operating conditions this light comes from multiple angles, increasing the reflection and parasitic absorption. Consequently, for every location, the double textured tandem module has lower reflection than the rear-textured module as the front texture is effective at reducing reflection losses.

The system losses have increased since the cable and inverter losses are included for the outdoors simulation. The inverter has a DC to AC efficiency in the range of 93.7% to 95.5% under operating conditions, which causes an inverter loss relative to the incoming power in the order of 1–2% for the crystalline silicon module and 2–3% for the tandem modules. The efficiency of an inverter typically increases for a higher voltage, making the inverter more efficient for a larger irradiance. This explains the difference between the inverter losses in Delft and Lisbon.

To compare the performance under STC with the outdoor performance, the DC efficiencies should be compared. This can be calculated by adding the cable and inverter losses to the AC power. The efficiency of the crystalline silicon module decreases slightly for outdoor conditions. This is mainly due to an increase of optical and electrical losses, whereas the fundamental losses decrease. For the tandem PV modules, the outdoor efficiency is also lower compared to STC. This is caused by an increase of optical losses and the increase of mismatch losses.

4. Summary and conclusion

We introduced the PVMD Toolbox the first model, which can model PV Systems based on fundamental material parameters all the way to AC energy yield without input from fabricated devices. We validated EQE and JV curves from labs cells with mean absolute deviation of 1.1% and 1.6% respectively. As validation for the lab to outdoor transition, since there is no outdoor energy yield data available for tandem PV systems, we used measurements from c-Si modules, whose yield we can reproduce with root mean square difference of 4.5%.

In our case study, we compare two types of 2 Terminal perovskite silicon tandem modules with a reference c-Si module (module STC efficiency 20.9%) at STC and in four different climates. The main difference is that the first tandem module has a flat front side and a textured rear leading to a module STC efficiency of 27.7%, while the second tandem module has a texture on both the front and rear side leading to a module efficiency of 28.6% in STC. We show that tandem PV modules operate at 1–1.9 °C lower yearly irradiance weighted average

temperatures compared to c-Si. Moreover, we find that the lab performance of the simulated tandem system translates from the laboratory to outdoors. As the specific yields of the tandem systems are within -2.7% to +0.4% the reference c-Si System for all four simulated climates.

Using our loss analysis, we find that effect current mismatch is significant overestimated in pure optical studies. As they do not account for fill factor gains. Quantitively, we find a tandem module with a current missmatch of 7% loses only 1.2% of its own module power and 0.3% of the incoming power due to current missmatch for one year in Delft.

We demonstrated that the PVMD ᴛᴏᴏʟʙᴏx enables the energy yield prediction based on fundamental material parameters. This can speed up the development of perovskite/silicon tandem module and their optimization for different climates.

CRediT authorship contribution statement

M.R. Vogt: Writing – original draft, Visualization, Validation, Supervision, Software, Project administration, Methodology, Investigation, Formal analysis, Data curation, Conceptualization. **C. Ruiz Tobon:** Visualization, Software, Data curation. **A. Alcañiz:** Writing – review & editing, Validation, Software. **P. Procel:** Writing – review & editing, Validation. **Y. Blom:** Writing – original draft, Visualization, Software, Methodology, Investigation. **A. Nour El Din:** Visualization, Validation, Software, Conceptualization. **T. Stark:** Software. **Z. Wang:** Software. **E. Garcia Goma:** Software. **J.G. Etxebarria:** Software. **H. Ziar:** Supervision, Funding acquisition. **M. Zeman:** Supervision. **R. Santbergen:** Writing – review & editing, Supervision, Software, Project administration, Funding acquisition, Conceptualization. **O. Isabella:** Supervision, Funding acquisition.

Declaration of competing interest

The authors declare that they have no known competing financial interests or personal relationships that could have appeared to influence the work reported in this paper.

Data availability

Data will be made available on request.

Acknowledgments

Appendix A. Simulated structures

Table A1 list the materials and thickness of all simulated structures.

Table A1
Full overview of the cell and module properties for 2T in air used for validation as well as the three encapsulated ones from the case study: The double textured c-Si as reference, the rear texture 2-Terminal tandem (2T-RT) and the double texture tandem (2T-DT). The silicon wafer thickness is fixed to 160 μm, which is a typical value for today's industrial c-Si solar cells, and the perovskite thickness is adjusted to achieve current matching in the module under STC.

	2T (cell in air)	c-Si (reference)	2T-RT	2T-DT
Glass DARC	Air	93 nm + 53 nm	93 nm + 53 nm	93 nm & 53 nm
Glass	Air	3.2 mm	3.2 mm	3.2 mm
Polyolefin	Air	450 μm	450 μm	450 μm
LiF	85 nm	NA	NA	NA
IZO	85 nm	NA	85 nm	85 nm

(continued on next page)

Table A1 (*continued*)

	2T (cell in air)	c-Si (reference)	2T-RT	2T-DT
SnO_2	5 nm	NA	5 nm	5 nm
C60	7 nm	NA	7 nm	7 nm
Perovskite	532 nm	NA	575 nm	480 nm
PTAA	23 nm	NA	23 nm	23 nm
ITO	63 nm	63 nm	63 nm	63 nm
nc-Si	111 nm	20 nm	111 nm	111 nm
a-Si(i)	9 nm	9 nm	9 nm	9 nm
Front texture	No	Yes	No	Yes
c-Si	300 μm	160 μm	160 μm	160 μm
Rear texture	Yes	Yes	Yes	Yes
a-Si(i)	6 nm	6 nm	6 nm	6 nm
a-Si(p)	12 nm	12 nm	12 nm	12 nm
AZO	55 nm	55 nm	55 nm	55 nm
Ag	300 nm	300 nm	300 nm	300 nm

References

[1] C. Breyer, et al., Solar photovoltaics demand for the global energy transition in the power sector, Prog. Photovoltaics Res. Appl. 26 (8) (2018) 505–523, https://doi.org/10.1002/pip.2950.

[2] N.M. Haegel, et al., Terawatt-scale photovoltaics: transform global energy, Science 364 (6443) (May 2019) 836–838, https://doi.org/10.1126/science.aaw1845.

[3] J.C. Goldschmidt, L. Wagner, R. Pietzcker, L. Friedrich, Technological learning for resource efficient terawatt scale photovoltaics, Energy Environ. Sci. (2021), https://doi.org/10.1039/D1EE02497C.

[4] VDMA, International Technology Roadmap for Photovoltaic (ITRPV) 2020 Results, 2021.

[5] IEC61836: Solar Photovoltaic Energy Systems - Terms, Definitions and Symbols, 2016.

[6] K. Yoshikawa, et al., Silicon heterojunction solar cell with interdigitated back contacts for a photoconversion efficiency over 26, Nat. Energy 2 (5) (May 2017) 17032, https://doi.org/10.1038/nenergy.2017.32.

[7] M.A. Green, Y. Hishikawa, E.D. Dunlop, D.H. Levi, J. Hohl-Ebinger, A.W.Y. Ho-Baillie, Solar cell efficiency tables (version 51), Prog. Photovoltaics Res. Appl. 26 (1) (Jan. 2018) 3–12, https://doi.org/10.1002/pip.2978.

[8] A. Richter, M. Hermle, S.W. Glunz, Reassessment of the limiting efficiency for crystalline silicon solar cells, IEEE J. Photovoltaics 3 (4) (Oct. 2013) 1184–1191, https://doi.org/10.1109/JPHOTOV.2013.2270351.

[9] B.A. Veith-Wolf, S. Schäfer, R. Brendel, J. Schmidt, Reassessment of intrinsic lifetime limit in n-type crystalline silicon and implication on maximum solar cell efficiency, Sol. Energy Mater. Sol. Cell. 186 (Nov. 2018) 194–199, https://doi.org/10.1016/j.solmat.2018.06.029.

[10] M. Jošt, L. Kegelmann, L. Korte, S. Albrecht, Monolithic perovskite tandem solar cells: a review of the present status and advanced characterization methods toward 30% efficiency, Adv. Energy Mater. 10 (26) (Jul. 2020), 1904102, https://doi.org/10.1002/aenm.201904102.

[11] EPFL and CSEM smash through the 30% efficiency barrier for perovskite-on-silicon-tandem solar cells—setting two certified world records, Press release (Jul. 07) (2022) 4.

[12] M.H. Futscher, B. Ehrler, Modeling the performance limitations and prospects of perovskite/Si tandem solar cells under realistic operating conditions, ACS Energy Lett. 2 (9) (Sep. 2017) 2089–2095, https://doi.org/10.1021/acsenergylett.7b00596.

[13] O. Dupré, B. Niesen, S. De Wolf, C. Ballif, Field performance versus standard test condition efficiency of tandem solar cells and the singular case of perovskites/silicon devices, J. Phys. Chem. Lett. 9 (2) (Jan. 2018) 446–458, https://doi.org/10.1021/acs.jpclett.7b02277.

[14] K. Jäger, P. Tillmann, E.A. Katz, C. Becker, Perovskite/silicon tandem solar cells: effect of luminescent coupling and bifaciality, Sol. RRL 5 (3) (Mar. 2021), 2000628, https://doi.org/10.1002/solr.202000628.

[15] PVsyst [Online]. Available: https://www.pvsyst.com/.

[16] HelioScope, Folsom labs [Online]. Available: https://www.helioscope.com/.

[17] Solar Monkey [Online]. Available: https://www.solarmonkey.nl/.

[18] Plant predict, First solar [Online]. Available: https://www.plantpredict.com/.

[19] PV*Sol, Valentin software GmbH [Online]. Available: https://www.valentin-software.com/en/products/photovoltaics/57/pvsol-premium.

[20] System advisor model, NREL [Online]. Available: https://sam.nrel.gov.

[21] P. Tillmann, K. Jäger, A. Karsenti, L. Kreinin, C. Becker, Model-chain validation for estimating the energy yield of bifacial perovskite/silicon tandem solar cells, Solar RRL (Jun. 2022), 2200079, https://doi.org/10.1002/solr.202200079.

[22] M.T. Hörantner, H.J. Snaith, Predicting and optimising the energy yield of perovskite-on-silicon tandem solar cells under real world conditions, Energy Environ. Sci. 10 (9) (2017) 1983–1993, https://doi.org/10.1039/C7EE01232B.

[23] N. Tucher, et al., Energy yield analysis of textured perovskite silicon tandem solar cells and modules, Opt Express 27 (20) (Sep. 2019) A1419, https://doi.org/10.1364/OE.27.0A1419.

[24] M. Singh, R. Santbergen, I. Syifai, A. Weeber, M. Zeman, O. Isabella, Comparing optical performance of a wide range of perovskite/silicon tandem architectures under real-world conditions, Nanophotonics 10 (8) (Jun. 2021) 2043–2057, https://doi.org/10.1515/nanoph-2020-0643.

[25] R. Schmager, M. Langenhorst, J. Lehr, U. Lemmer, B.S. Richards, U.W. Paetzold, Methodology of energy yield modelling of perovskite-based multi-junction photovoltaics, Opt Express 27 (8) (Apr. 2019) A507, https://doi.org/10.1364/OE.27.00A507.

[26] EYcalc [Online]. Available: https://github.com/PerovskitePV/EYcalc.

[27] A. Julien, J.-B. Puel, P. Lopez-Varo, J.-F. Guillemoles, S. Collin, Backside light management of 4-terminal bifacial perovskite/silicon tandem PV modules evaluated under realistic conditions, Opt Express 28 (25) (Dec. 2020), 37487, https://doi.org/10.1364/OE.405713.

[28] W. Shockley, H.J. Queisser, Detailed balance limit of efficiency of p-n junction solar cells, J. Appl. Phys. 32 (3) (1961) 510, https://doi.org/10.1063/1.1736034.

[29] M. Jošt, et al., Textured interfaces in monolithic perovskite/silicon tandem solar cells: advanced light management for improved efficiency and energy yield, Energy Environ. Sci. 11 (12) (2018) 3511–3523, https://doi.org/10.1039/C8EE02469C.

[30] Gueymard - Simple Model for the Atmospheric Radiative Transfe.Pdf.".

[31] Gueymard - 2001 - Parameterized Transmittance Model for Direct Beam .Pdf.".

[32] R. Santbergen, T. Meguro, T. Suezaki, G. Koizumi, K. Yamamoto, M. Zeman, GenPro4 optical model for solar cell simulation and its application to multijunction solar cells, IEEE J. Photovoltaics 7 (3) (May 2017) 919–926, https://doi.org/10.1109/JPHOTOV.2017.2669640.

[33] R. Siegel, Net radiation method for transmission through partially transparent plates, Sol. Energy 15 (3) (1973) 273–276, https://doi.org/10.1016/0038-092X(73)90090-X.

[34] R. Santbergen, R.J.C. van Zolingen, The absorption factor of crystalline silicon PV cells: a numerical and experimental study, Sol. Energy Mater. Sol. Cell. 92 (4) (Apr. 2008) 432–444, https://doi.org/10.1016/j.solmat.2007.10.005.

[35] R. Santbergen, J.M. Goud, M. Zeman, J.A.M. van Roosmalen, R.J.C. van Zolingen, The AM1.5 absorption factor of thin-film solar cells, Sol. Energy Mater. Sol. Cell. 94 (5) (May 2010) 715–723, https://doi.org/10.1016/j.solmat.2009.12.010.

[36] K. Jäger, M. Fischer, R.A.C.M.M. van Swaaij, M. Zeman, A scattering model for nano-textured interfaces and its application in opto-electrical simulations of thin-film silicon solar cells, J. Appl. Phys. 111 (8) (Apr. 2012), 083108, https://doi.org/10.1063/1.4704372.

[37] M. Zeman, O. Isabella, S. Solntsev, K. Jäger, Modelling of thin-film silicon solar cells, Sol. Energy Mater. Sol. Cell. 119 (Dec. 2013) 94–111, https://doi.org/10.1016/j.solmat.2013.05.037.

[38] R. Santbergen, et al., ASA Software for Opto-Electrical Simulation of Silicon, CIGS and Perovskite Solar Cells, 2019. Xi'an (China).

[39] ASA web simulator [Online]. Available: https://asa.ewi.tudelft.nl/.

[40] R. Santbergen, V.A. Muthukumar, R.M.E. Valckenborg, W.J.A. van de Wall, A.H.M. Smets, M. Zeman, Calculation of irradiance distribution on PV modules by combining sky and sensitivity maps, Sol. Energy 150 (Jul. 2017) 49–54, https://doi.org/10.1016/j.solener.2017.04.036.

[41] R. Perez, R. Seals, J. Michalsky, All-weather model for sky luminance distribution—preliminary configuration and validation, Sol. Energy 50 (3) (Mar. 1993) 235–245, https://doi.org/10.1016/0038-092X(93)90017-I.

[42] C. Gueymard, "Simple Model for the Atmospheric Radiative Transfer of Sunshine (SMARTS2) Algorithms and Performance Assessment," p. 84.

[43] C.A. Gueymard, Parameterized transmittance model for direct beam and circumsolar spectral irradiance, Sol. Energy 71 (5) (Nov. 2001) 325–346, https://doi.org/10.1016/S0038-092X(01)00054-8.

[44] M.K. Fuentes, A simplified thermal model for flat-plate photovoltaic arrays, SAND-85-0330, https://www.osti.gov/biblio/6802914, 1987 [Online]. Available:.

[45] A. Jain, Exact analytical solutions of the parameters of real solar cells using Lambert W-function, Sol. Energy Mater. Sol. Cell. 81 (2) (Feb. 2004) 269–277, https://doi.org/10.1016/j.solmat.2003.11.018.

[46] W. Boyson, G. Galbraith, D. King, S. Gonzalez, Performance Model for Grid-Connected Photovoltaic Inverters, Sep. 2007, 920449, https://doi.org/10.2172/920449. SAND2007-5036.

[47] T. Stark, Modeling and Monitoring of a Floating Photovoltaic Pilot System, MSc Thesis, TU Delft, 2020.

[48] World record again at HZB: almost 30 % efficiency for next-generation tandem solar cells [Online]. Available: https://www.helmholtz-berlin.de/pubbin/news_seite?nid=23248;sprache=en;seitenid=1, Nov. 22, 2021.

[49] Oxford PV hits new world record for solar cell, Press release, Dec. 21, https://www.oxfordpv.com/news/oxford-pv-hits-new-world-record-solar-cell#:~:text=Revolutionary%20perovskite%20solar%20technology%20has,of%20solar%20energy%20into%20electricity, 2020 [Online]. Available:.

[50] A. Al-Ashouri, et al., Monolithic perovskite/silicon tandem solar cell with >29% efficiency by enhanced hole extraction, Science 370 (6522) (Dec. 2020) 1300–1309, https://doi.org/10.1126/science.abd4016.

[51] B. Marion, M.G. Deceglie, T.J. Silverman, Analysis of measured photovoltaic module performance for Florida, Oregon, and Colorado locations, Sol. Energy 110 (Dec. 2014) 736–744, https://doi.org/10.1016/j.solener.2014.10.017.

[52] M.R. Vogt, et al., Measurement of the optical constants of soda-lime glasses in dependence of iron content and modeling of iron-related power losses in crystalline Si solar cell modules, IEEE J. Photovoltaics 6 (1) (Jan. 2016) 111–118, https://doi.org/10.1109/JPHOTOV.2015.2498043.

[53] J.H. Lowry, Optical characteristics of Teflon AF fluoroplastic materials, Opt. Eng. 31 (9) (1992) 1982, https://doi.org/10.1117/12.59910.

[54] M.K. Yang, Optical properties of Teflon® AF amorphous fluoropolymers, J. Nanolithogr. MEMS, MOEMS 7 (3) (Jul. 2008), 033010, https://doi.org/10.1117/1.2965541.

[55] M.R. Vogt, Development of Physical Models for the Simulation of Optical Properties of Solar Cell Modules, doctoral thesis, Gottfried Wilhelm Leibniz Universität Hannover, Hannover, 2015, https://doi.org/10.15488/8592 [Online]. Available:.

[56] A.D. Vos, Detailed balance limit of the efficiency of tandem solar cells, J. Phys. D Appl. Phys. 13 (5) (May 1980) 839–846, https://doi.org/10.1088/0022-3727/13/5/018.

[57] F. Urbach, The long-wavelength edge of photographic sensitivity and of the electronic absorption of solids. https://doi.org/10.1103/PhysRev.92.1324, 1953, 1.

[58] J. Ascencio-Vásquez, K. Brecl, M. Topič, Methodology of Köppen-Geiger-Photovoltaic climate classification and implications to worldwide mapping of PV system performance, Sol. Energy 191 (Oct. 2019) 672–685, https://doi.org/10.1016/j.solener.2019.08.072.

[59] W. Koeppen, Klassifikation der Klimate nach Temperatur, Niederschlag und Jahresablauf, Petermanns Geogr. Mittl. (1918) 193–203.

[60] M.C. Peel, B.L. Finlayson, T.A. McMahon, Updated world map of the Köppen-Geiger climate classification, Hydrol. Earth Syst. Sci. 11 (5) (Oct. 2007) 1633–1644, https://doi.org/10.5194/hess-11-1633-2007.

[61] J.S. Bartlett, Á.M. Ciotti, R.F. Davis, J.J. Cullen, The spectral effects of clouds on solar irradiance, J. Geophys. Res. 103 (C13) (Dec. 1998) 31017–31031, https://doi.org/10.1029/1998JC900002.

[62] C.R. Osterwald, K.A. Emery, M. Muller, Photovoltaic module calibration value versus optical air mass: the air mass function: PV module calibration value versus optical air mass, Prog. Photovoltaics Res. Appl. 22 (5) (May 2014) 560–573, https://doi.org/10.1002/pip.2303.

[63] X. Liu, et al., Development of a fast and accurate PCRTM radiative transfer model in the solar spectral region, Appl. Opt. 55 (29) (Oct. 2016) 8236, https://doi.org/10.1364/AO.55.008236.

[64] H.H. Aumann, et al., Evaluation of radiative transfer models with clouds, J. Geophys. Res. Atmos. 123 (11) (Jun. 2018) 6142–6157, https://doi.org/10.1029/2017JD028063.